Research paper

Exfoliation and intercalation of montmorillonite by small peptides

Karin A. Block [a],[*], Adrianna Trusiak [a], Al Katz [b], Alexandra Alimova [c], Hui Wei [c], Paul Gottlieb [c], Jeffrey C. Steiner [a]

[a] Department of Earth and Atmospheric Sciences, The City College of New York, 160 Convent Ave, New York, NY 10031, United States
[b] Department of Physics, The City College of New York, 160 Convent Ave, New York, NY 10031, United States
[c] Sophie Davis School of Biomedical Education, The City College of New York, 160 Convent Ave, New York, NY 10031, United States

ABSTRACT

Understanding structural changes in clay minerals induced by complexation with organic matter is relevant to soil science and agricultural applications. In this study, the effect of peptide storage in montmorillonite and the thermal stability of peptide–clay complexes were examined through characterization by X-ray diffraction (XRD), electron microscopy, UV absorption, and thermogravimetric analysis (TGA). XRD analysis of small peptide–montmorillonite clay complexes produced profiles consisting of reflections associated with the smectite 001 reflection and related peaks similar to that produced by a mixed layer clay mineral structure. Shifts in higher order diffraction maxima were attributed to disorder caused by the intercalation with the peptides. Increasing peptide concentrations resulted in greater shifts toward smaller 2θ from $6.37°$ (1.39 nm) to $5.45°$ (1.62 nm) as the interlayer space expanded. The expansion was accompanied by broadening of the 001 reflection (FWHM increases from 0.51 to $1.22°$ 2θ). The XRD line broadening was interpreted as caused by poorer crystallinity resulting from intercalation and tactoid exfoliation. SEM images revealed montmorillonite platelets with upwardly rolled edges that tend toward cylindrical structures with the production of tubules. High-resolution TEM images revealed bending of montmorillonite platelets, confirming exfoliation. The distribution of basal spacings in the micrographs was determined from the spatial frequencies obtained by Fourier analysis of density profiles. The distribution indicated the presence of discrete coherent crystallite domains. XRD and TGA results indicated that higher peptide concentrations resulted in a greater fraction of intercalated peptides and that surface adsorption of peptides mediated intercalation. Therefore, higher peptide concentration led to more stable organoclay complexes. However, UV absorption and TGA found that peptide adsorption onto montmorillonite had a finite limit at approximately 16% by weight.

© 2015 Elsevier B.V. All rights reserved.

1. Introduction

Poorly crystalline minerals, i.e., clays, protect soil organic matter (OM) produced by leaf and root litter from microbial degradation (Kleber et al., 2005). The persistence of smaller peptides in association with clays has been acknowledged as possibly leading to longer residence times for soil carbon and nitrogen (Kleber et al., 2007).

The mineral fraction in soils has been shown to enhance chemical recalcitrance in the degradation of OM (Eusterhues et al., 2003), lending stability to the carbon reservoir in old soils. This has implications for the global carbon cycle and for clay-mediated storage of nutrients in soils at extended time scales. However, the role of peptides in association with minerals and their relative contribution to the stabilization of carbon in soils are poorly understood (Kleber et al., 2007). The structure of clays, and its role in stabilizing carbon and nitrogen from peptides may be important in estimating turnover time of soil OM (Rillig et al., 2007).

Clays are able to react with amino acids and other organic molecules forming organoclays (Greenland et al., 1965a,b; Harter and Stotzky, 1971). Organoclays mediate the relationship of microbes to soils and sediments and may have played a role in the development of prebiotic life (Bouchoucha et al., 2011; Carneiro et al., 2011a,b; Fraser et al., 2011; Georgelin et al., 2013). Conversely, organic molecules may modify the structure of clays. For example, microbes are known to play a role in the smectite to illite transition (Kim et al., 2004; Zhang et al., 2007a,b; Jaisi et al., 2011).

Smectites are highly reactive and possess an overall negative charge under ordinary critical zone conditions. The interlayer space cations in smectites can be readily exchanged with positively charged or polar molecules, including organics, to create intercalated and pillared structures (Bergaya and Lagaly, 2013). Montmorillonite (Mt), a common smectite clay, can form organoclay complexes with proteins, enhancing the retention of organic matter in soil (Mayer, 1994; Sollins et al., 1996; Sheng et al., 2001). At near neutral pH, smectite platelets have negatively charged faces and positively charged edges, thus, smectites may potentially interact electrostatically with charged amino acids (Hedges and Hare, 1987; Senwo and Tabatabai, 1998; Benincasa et al., 2000; Laird et al., 2001; Benetoli et al., 2007; Carneiro et al., 2011a,b).

Smectites may also potentially interact with either the amide or carboxyl terminus of non-charged amino acids. Adsorption of different combinations of amino acids by smectites is known to be influenced by interlayer space cations (Arfaioli et al., 1999; Benincasa et al., 2000).

While large proteins can be adsorbed on the surface of clays where they are protected from enzymatic degradation (Theng, 1982), the products of degradation, such as peptides and amino acids, favor the possibility of absorption into the smectite interlayer space due to their smaller size. Kalra et al. (2003) utilized UV spectroscopy to investigate the adsorption of simple peptides onto divalent cation exchanged Mt. They determined that peptide adsorption is maximal at neutral pH and 23 °C and was greatest for glycine tetramers followed by glycine trimers and glycine–alanine dimers. The glycine dimers showed the lowest adsorbability.

Effenberger et al. (2009) found that the intercalation of Mt with alanine, leucine or phenylalanine produced a modified Mt with an increased d_{001}-spacing. Kollár et al. (2003) ion-exchanged several amino acids into Na-Mt and verified by Fourier transform infrared spectroscopy and XRD that the amino acids were successfully intercalated. Parbhakar et al. (2007) examined adsorption of L-lysine onto smectites and discussed the potential role of clays in promoting catalytic reactions in organic compounds. Naidja and Huang (1994) observed that aspartic acid absorption into Ca-Mt is a fast reaction process with 84% of the aspartic acid absorbed (56.2 μmol/g clay); the d_{001} spacing of the aspartic acid–Mt complex decreased at temperatures above 150 °C. They found that the aspartic acid appeared weakly bound to the surface indicating that it intercalated in the Mt through a water bridge.

The majority of the studies on smectite–amino acid interactions have focused on the effects that smectites have on amino acids and proteins (Bujdák et al., 1996; Lagaly, 2006; Lambert, 2008; Yu et al., 2013; Jaber et al., 2014). There have been fewer investigations into the changes that occur in the smectite structure as a result of amino acid, peptide or protein intercalation. Nonetheless, it is known that adsorption onto the surface or into the interlayer space plays a significant role in forming clay–protein complexes (Theng, 2012). To examine the role of mineral structure in the formation of peptide–clay complexes tryptone was utilized as a peptide source. Tryptone is a casein pancreatic digest which contains all twenty amino acids in peptide form. Tryptone oligomers consist mostly of monomers, dimers, trimers, and tetramers; therefore it is an excellent source of small peptides of multiple amino acids that makes it suitable for experiments with clay.

In this paper, the incorporation of suites of small oligopeptides, which are the products of OM decomposition, into Mg-Mt is examined by measuring the effect of peptides on clay structure, and determining the thermal stability of organo-clay complexes. The results of X-ray diffraction (XRD), high-resolution transmission electron microscopy (HRTEM) and thermogravimetric analysis (TGA) experiments that demonstrate the nature of the interactions are presented. XRD is compared to HRTEM data to determine the effect of adsorption on clay crystallinity at the bulk and local scales. TGA was utilized to ascertain the effect of peptide concentration on adsorption. As a conclusion, the results are placed in the context of the existing models for OM adsorption.

2. Materials and methods

2.1. Sample preparation

2.1.1. Montmorillonite

A high purity dioctahedral Mt ($(Na,Ca)_{0.33}(Al_{1.67}Mg_{0.33})Si_4O_{10}(OH)_2 \cdot nH_2O$; source: Belle Fourche, South Dakota, USA) — commercial name Volclay Accofloc 350 (American Colloid Company, Arlington Heights, IL) was made homoionic with magnesium through the cation substitution technique of Moore and Reynolds (1997). Accofloc is known to have a cation exchange capacity (CEC) of 79 meq/100 g (Sterte and Shabtai, 1987). The clay was initially washed in 5% sodium hypochlorite

to remove organic contaminants, followed by a triple wash in distilled water to remove the sodium hypochlorite. Large clay particles and non-clay minerals were removed by centrifugation at 1200 rpm (235 g) for 5 min. The supernatant comprising the fraction smaller than 2 μm was collected. The purified clay was suspended in 0.1 M MgCl₂ overnight and centrifuged at 3600 rpm (2100 g) for 30 min. The pellet was vortexed, rinsed in distilled water 8–10 times, and then resuspended in distilled water. Two drops of AgNO₃ were added to the suspension after the rinses to verify that all chloride was removed. The suspension was then autoclaved at 122 °C and 0.103 MPa for 15 min to ensure sterility. The concentration (w/v) of the stock Mt suspension is 6.0 mg/ml. Visual inspection of the Mt suspension indicated no noticeable settling or aggregation during storage.

2.1.2. Tryptone Mt aggregates

Tryptone consists of oligomers, 50% of which have a molecular mass less than 500 Da; 33% are monomers, and only 10% of the peptides have a molecular mass greater than 2 kDa. A complete compositional breakdown of tryptone was obtained from the vendor website (Bacto-tryptone, Becton Dickinson; San Jose, CA; URL: http://www.bd.com/ds/technicalCenter/). Typical certificate of analysis values reported by the vendor are less than 8% ash, 13.8% nitrogen (Kjeldahl), and 6.6% amino nitrogen (modified Sorensen). Tryptone stock solutions were prepared by dissolving tryptone powder in distilled water at a concentration of 0.1 g/ml followed by autoclaving at 122 °C and 0.103 MPa for 15 min. Tryptone Mt aggregates (Mt_{TP}) were prepared by mixing 9 ml of Mt suspension with 1 ml of dilutions of the tryptone stock to give tryptone concentrations ranging from 0.5 mg/ml to 10 mg/ml mixed with 5.4 mg/ml of Mt in 10 ml suspensions. Aggregates were allowed to stand for up to 72 h prior to acquiring the XRD pattern. The aggregates were centrifuged at 3600 rpm (2700 g) for 10 min. The supernatant components were analyzed by optical absorption and the pellets collected for further analysis. For XRD analysis, the pellets were smeared on glass slides. Samples for SEM were fixed and mounted on aluminum stubs, coated with palladium–gold alloy. For HRTEM, pellets were vortexed and fixed in plastic resin (Leser et al., 2009). The resin samples were microtomed (UltraCut6 Ultramicrotome, Leica, Buffalo Grove, IL) to produce ~70 nm slices for HRTEM. The microtomed slices were placed on carbon-coated grids for TEM analysis.

2.2. X-ray diffraction

XRD patterns were acquired with a PANalytical X'Pert Pro equipped with a chromium cathode tube producing Cu Kα radiation at 1.5418 Å; a Ni foil filter to attenuate Cu Kβ emission; and a PixCel 1-D detector array. A divergence slit of 1/16th of a degree and an anti-scatter slit of 5.7 mm were used to minimize background scatter at low 2θ. Scans were run in the range of 4° to 35° 2θ at a step size of 0.007° and a scan rate of 0.35 steps/s.

2.3. UV absorption

UV absorption spectroscopy (Cary 500 UV–Vis absorption spectrophotometer, Agilent Technologies Inc., Foster City, CA) in the range of 250 to 300 nm was used to estimate the fraction of tryptone sorbed (intercalated or surface adsorbed) onto the Mt based on the relative optical absorption of the Mt_{TP} supernatant compared to a stock tryptone solution. The supernatant extinction spectra in the 400 to 700 nm range, a non-absorbing region for both Mt and tryptone, was used to estimate the scattering losses from (non-aggregated) Mt tactoids that remained in suspension. To keep the transmission above the noise, the supernatant was diluted 5×. Spectra were collected in 1 cm path length quartz cuvettes.

2.4. Electron microscopy

Scanning electron micrographs were acquired on a Zeiss Supra 55V scanning electron microscope (SEM) operating at 30 kV. The detector is a 768 × 1024 pixel CCD. HRTEM images were acquired with either: 1) a Tecnai F20 electron microscope (FEI Inc., Hillsboro, OR) operating at 200 kV with a TVIPS F415 4096 × 4096 pixel CCD (Tietz Video and Image Processing Systems GmbH, Gauting, Germany); or 2) a JEOL JEM2100 (JEOL Inc., Peabody, MA) operating at 200 kV with a Gatan Orius 2048 × 2048 pixel CCD (Gatan Inc., Pleasanton, CA). The effective pixel sizes are: 0.0297 nm/pixel at ×280,000 magnification (0.0594 nm/pixel after 2× binning) on the F20; and 0.034 nm/pixel at ×150,000 magnification on the JEM2100.

2.5. Thermogravimetric measurements

Thermogravimetric analysis was conducted on a TA Instruments Q500 TGA (New Castle, DE) and a Netzsch STA 409 PC Luxx TG/DTA/DSC (Netzsch Instruments, Boston, MA). Measurements were collected in a nitrogen atmosphere on the Q500 and argon atmosphere on the STA 409 at temperatures ranging from room temperature to 800 °C at a heating rate of 10 °C/min on the Q500 and 3 °C/min on the STA 409. Air dried Mt and Mt_{TP} samples of 25 mg were placed in alumina cups for individual runs. TGA data was utilized here to determine the relative percent peptide adsorbed on the surface of the clay and intercalated into the interlayer space. The dehydration and dehydroxylation temperatures of Mt and the temperature range of amino acid decomposition are well-known and were used to characterize the nature of the interaction between peptides and Mt (Olafsson and Bryan, 1970; Xi et al., 2004).

### 2.6. Image and data processing

XRD patterns were fitted to Lorentzian line shapes using the OriginPro (OriginLab, Northampton, MA) peak fitting function. Contrast enhancement of the micrographs was performed using the auto-adjust function of CorelDraw X4 Suite (Corel Corp. Ottawa, Canada). Fourier spatial frequency analysis was performed on density profiles of local-histogram-equalized segments of micrographs to compensate for spatial variation in electron beam intensity. The histogram equalization was done in order to reduce low spatial frequency components due to large-scale differences in density resulting from variation in sample thickness. Prior to Fourier analysis, plot profiles were adjusted to have zero average density thus reducing the Fourier D.C. component to zero.

3. Results and discussion

3.1. X-ray diffraction

Intercalation of small peptides in the Mt expanded the interlayer space as evidenced by shifts in the 001 XRD reflections to smaller 2θ. The extent of basal spacing expansion increased with greater tryptone concentration and/or longer intercalation time. The XRD patterns (4.5° to 8° 2θ Cu Kα) from the Mt control (hydrated) and Mt_{TP} solution at tryptone concentrations of 1, 2.5, 5 and 10 mg/ml are shown in Fig. 1a. Least squares Lorentzian fits to the 001 reflection are plotted (dotted lines). The 001 reflections and corresponding FWHM are listed in Table 1. The changes in 001 reflection angle in the patterns indicate that the d-spacing increased as a function of tryptone concentration and mixing time. For concentrations of tryptone greater than 1 mg/ml, the XRD patterns of peptide-intercalated Mt exhibited diminished intensity and line broadening of rational reflections.

Higher order XRD reflections from oriented mounts are at approximate multiples of the 2θ angle of the 001 reflection, but for the intercalated clays, the scattering angles of higher order reflections revealed further details (Moore and Reynolds, 1997). The XRD patterns (4.5° to 35° 2θ) for the Mt control and Mt mixed with 5 and 10 mg/ml tryptone solutions (Mt_{TP-5} and Mt_{TP-10}, respectively) are shown in Fig. 1b. For the Mt control, the higher order reflection angles were near multiples of the 001 reflection angle — indicative of a purified Mg-clay structure mounted in the 00l preferred orientation. In the patterns from tryptone-intercalated Mt, higher order reflections were shifted and broadened. Several distinct new reflections, as well as 'shoulders' appeared at non-multiples of 2θ for the 001 reflection, and were especially visible in Mt_{TP-10}. The broadening of the XRD reflections in the Mt represents a combination of smaller particle size and the presence of smaller volumes of coherent crystallite domains. The Scherrer equation (Jonas and Oliver, 1967), which gives the mean particle size or the size of coherent crystallite domains on the basis of line broadening, yielded an average crystallite domain thickness of 7 nm for intercalated clay and 17 nm for the unmodified Mt. This suggests that ordered structures extended for significantly smaller domains in the intercalated samples than in the control. The shoulder at approximately 10° 2θ suggests that some of the crystallite domains lacked tryptone and contained little interlayer space water, and existed in sufficient amounts to be visible above background (although barely). The resulting non-periodic structure was manifested as a convolution of the higher order 00l reflections, a significant shift in the position of the 001 reflection indicating expansion of the interlayer space, and broadening of the of the 00l reflections
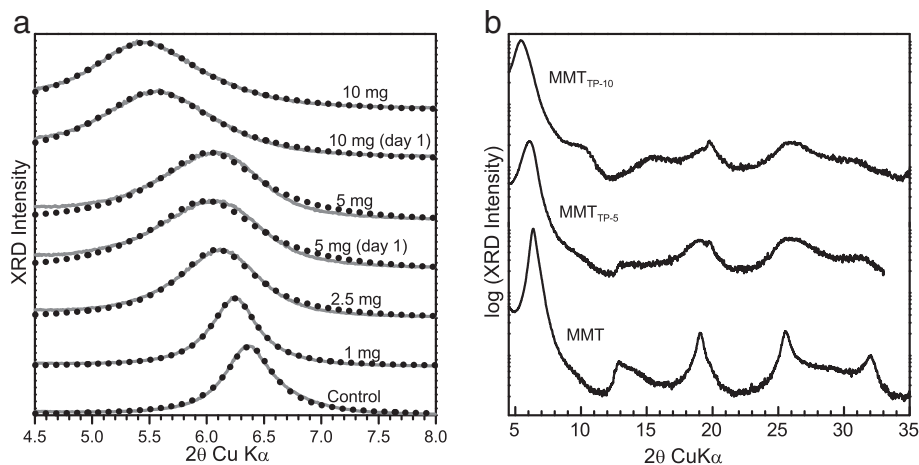
Fig. 1. a) XRD 001 reflections from Mt and Mt_{TP} with corresponding single-peak Lorentzian least-squares fits. Tryptone and Mt were allowed to mix for 3 days except as noted; b) XRD patterns from 4.5° to 35° 2θ showing higher order reflections. Mt control reflections are close to multiples of the 001 reflection but for Mt_{TP}, higher order reflections do not align with multiples of 2θ for the d_{001} reflection and several additional peaks are present.

Table 1
XRD 001 reflections of Mt$_{TP}$.

Tryptone concentration (mg/ml)	Intercalation time (days)	001 reflection maximum (°2θ)	001 reflection FWHM (°2θ)	d_{001}-Value (nm)
0	–	6.37	0.51	1.39
1	3	6.23	0.49	1.42
2.5	3	6.09	0.85	1.45
5	1	5.99	1.16	1.48
5	3	6.02	1.11	1.47
10	1	5.54	1.30	1.60
10	3	5.45	1.22	1.62

due to smaller volumes of coherent order among the atoms in the tryptone-clay.

3.2. UV absorption

The amount of peptides sorbed onto the Mt was estimated from UV absorption. In the 250 to 300 nm spectral range, protein absorption is due to the aromatic amino acids — primarily tryptophan and tyrosine (Stoscheck, 1990). In the 400 to 700 nm range, both Mt and proteins are non-absorbing, therefore optical extinction is due to scattering losses. Using the Rayleigh–Gans–Debye theory (Xu, 2003; Xu et al., 2003; Xu and Katz, 2008), the extinction losses in the visible wavelength range were used to estimate scattering losses in the 250 to 300 nm wavelength range. This analysis also indicated that approximately 0.3 mg/ml of the Mt (the non-aggregated small fraction, <0.2 μm) remained in the supernatant from an initial concentration of 5.4 mg/ml. The scattering losses were then subtracted from the UV optical extinction to determine optical absorption due to proteins and thus protein concentration in the supernatants. The UV absorption data (not shown) indicated that 90% of the tryptone remained in the supernatant and 10% (1 mg/ml) was absorbed onto the Mt$_{TP-10}$ sample. Therefore the Mt$_{TP-10}$ aggregates were 84% Mt and 16% tryptone, by mass. Analysis

of the Mt$_{TP-5}$ supernatant spectra indicated that the Mt$_{TP-5}$ aggregates were 85% Mt and 15% tryptone, by mass.

3.3. SEM

A wide-field SEM micrograph (×67,000 magnification; 4.55 μm field of view) of a Mt$_{TP}$ aggregate showing many Mt tactoids is presented in Fig. 2a. Many of the platelets exhibit curling at the platelet edges; black arrows point to platelet edges where the curling is extensive and exemplified by the isolated platelet located near the center of the micrograph. Smaller platelets tended to form cylindrical tubules (white arrows in Fig. 2a indicate some of the tubules). A higher magnification (×434,000) SEM micrograph corresponding to the boxed region in Fig. 2a is presented in the Fig. 2b micrograph. The single Mt$_{TP}$ tactoid in this micrograph has both left-side and right-side edges rolled approximately 180° and less substantial curling at the top and bottom right. Edge curling in clays has been documented for kaolinites, and less extensively for smectites, and is regarded as the result of tactoid exfoliation due to intercalation (Keller et al., 1986; Lee and Kim, 2002a, b). A wide field micrograph consisting of individual tactoids of untreated Mt is shown in Fig. 2c. The central tactoid is shown in Fig. 2d at higher magnification. None of the tactoids in the micrograph exhibited curling.

3.4. TEM

Curling of the Mt tactoids increased the probability of observing, via HRTEM, edge-on orientation in an arbitrarily microtomed pellet. Nonetheless, the incidence of edge-on tactoids was uncommon. In this study, thirty electron micrographs were collected that exhibited clearly defined edge-on orientations suitable for analysis of basal layer thickness. In micrographs of curled tactoids, the platelet layers were observable near the particle edges with alternating 2:1 tetrahedral–octahedral–tetrahedral (T–O–T) sheets and interlayer space bands with the T–O–T sheets darker and interlayer spaces lighter. Although determination of basal spacing by TEM analysis is less precise than XRD analysis, it provides local sampling while XRD gives a volume
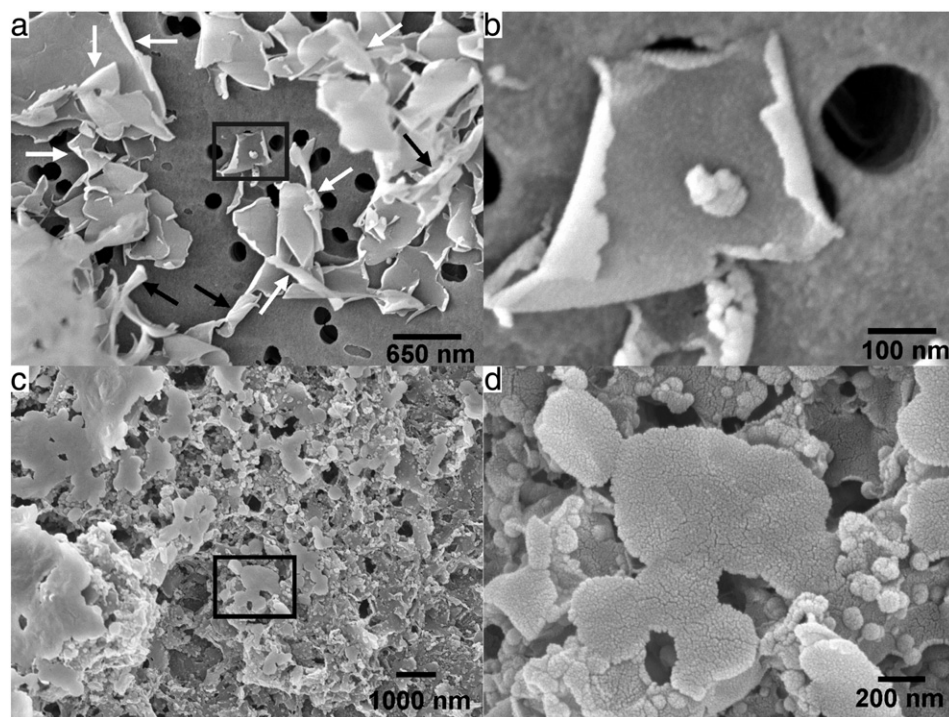
Fig. 2. a) Wide field SEM of Mt$_{TP}$ with white arrows indicating regions with curled edges and black arrows identifying cylindrical tubules. b) Higher magnification micrograph of tactoids in the central (boxed) region of panel a; substantial curling of the tactoid edges is evident on the right and left sides and, to a lesser extent, on the top center and bottom right; c) wide field SEM of Mt control, no edge curling is evident in the tactoids; d) higher magnification micrograph of tactoids in central (boxed) region of Mt control shown in c.
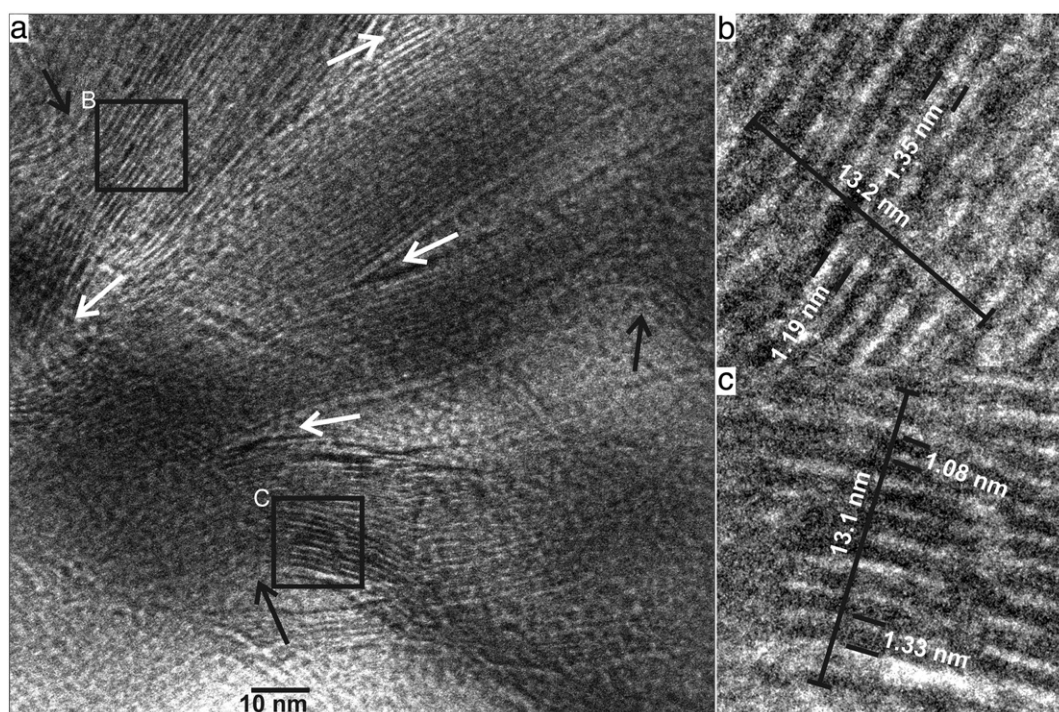
Fig. 3. a) HRTEM of Mt$_{TP-10}$. White arrows indicate regions of branching and black arrows indicate curling/exfoliation of layers. b, c) Enlarged insets showing variation of basal spacing. Lines extend across 10 platelets.

average. TEM analysis highlights the short-range structural variability of tactoids.

The layered structure of the Mt$_{TP}$ tactoid is observable in HRTEM micrographs (Fig. 3a) throughout the clay as evidenced by quasi-parallel bands. In several regions of the micrograph (white arrows), the tactoids exhibited splitting — an indication of exfoliation. Regions in which the platelets appear curved are indicated by black arrows. Close examination of the micrograph shows that there is a large variation in the width of the dark and light pairs — consistent with the broad XRD patterns for the intercalated Mt. Two regions labeled B and C were
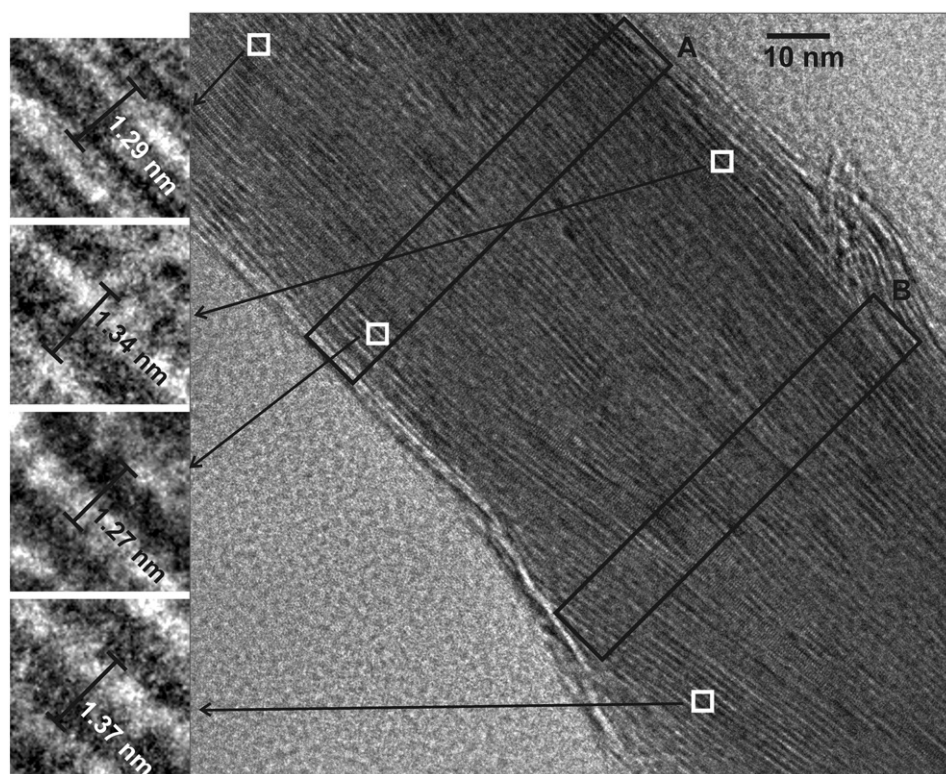
Fig. 4. HRTEM micrograph of Mt$_{TP-10}$ showing a thick tactoid edge-on exhibiting characteristic quasi-parallel layering. Insets from several regions of micrograph show variation in interlayer space thickness.

chosen because: 1) they exhibited high contrast between the interlayer spaces and the T–O–T sheets; and 2) they contained a large number of parallel platelets, allowing layer thickness to be averaged over ten adjacent platelets (enlarged in Fig. 3 insets b and c, respectively). A large variation in basal spacing from 1.08 to 1.35 nm was observed in the insets. This is consistent with broadening of the XRD patterns of intercalated Mt. In order to improve the accuracy of distance estimates in the micrographs, the average basal spacing taken over 10 bands was measured in two sections. The average spacing is 1.31 nm for each of the sections (Fig. 3 insets b and c). It is noted that the d_{001} spacing as measured by TEM is less than the value obtained by XRD, evidence that resin fixation during TEM sample preparation reduced the interlayer space thickness, possibly a result of dehydration.

An HRTEM micrograph of a Mt_{TP-10} tactoid containing approximately 55 layers is shown in Fig. 4. Note that this sample was atypical in that most of the observed tactoids in the micrographs exhibited significantly more splitting and curling (see Fig. 3a). Nonetheless, central portions of the tactoid exhibited pinching out of layers and discontinuities along the length of the tactoid. The Mt_{TP} exhibited local variation in the basal thickness (Fig. 4, insets). As the T–O–T sheets do not vary in thickness, the observed variation is most likely due to variation in interlayer space thickness. The large number of quasi-parallel layers facilitated the generation of density profiles of regions transverse to the layers and determination of basal spacing by Fourier analysis. The density profiles after local-histogram-equalization of two representative transverse regions, labeled A and B, are plotted in Fig. 5a. Because higher electron dense regions (e.g., T–O–T sheets) are darker in EM micrographs, they exhibit lower values in plot profiles than less electron dense regions (e.g., interlayer space). The power spectra, showing the spatial frequencies of the profiles are plotted in Fig. 5b. The Fourier analysis indicated a non-random distribution of layer thicknesses. Region A manifested more uniformity in the profile spacing and light/dark band contrast than region B, indicating larger coherent domains and greater homogeneity. The region A spectrum exhibited a higher magnitude, narrower peak centered at 0.784 nm^{-1} (d_{001}-value = 1.28 nm) and a lower

Fig. 6. HRTEM of Mt_{TP} intercalated with 0.5 mg/ml of tryptone showing tactoid edge-on. Nearly continuous layering at the left, right and top edges is clearly visible.

magnitude peak at 0.840 nm^{-1} (d_{001}-value = 1.19 nm). This bimodal distribution may have arisen from a mixture of intercalated and non-intercalated domains. The non-intercalated layers were highly contracted due to water loss during sample preparation, while the intercalated layers exhibited some contraction from water loss. However, the interlayer
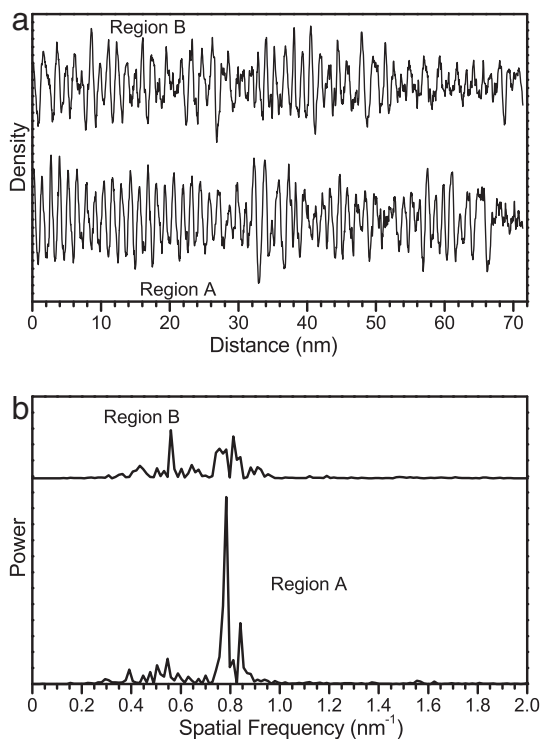

Fig. 5. a) Density profile of Fig. 4 regions A and B. Distances start at left edges of rectangles. b) Power spectra of density profiles plotted in panel a.
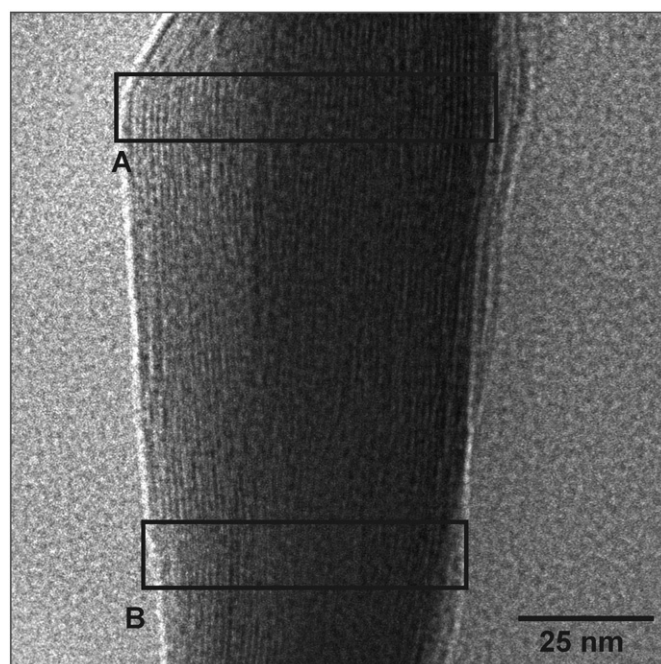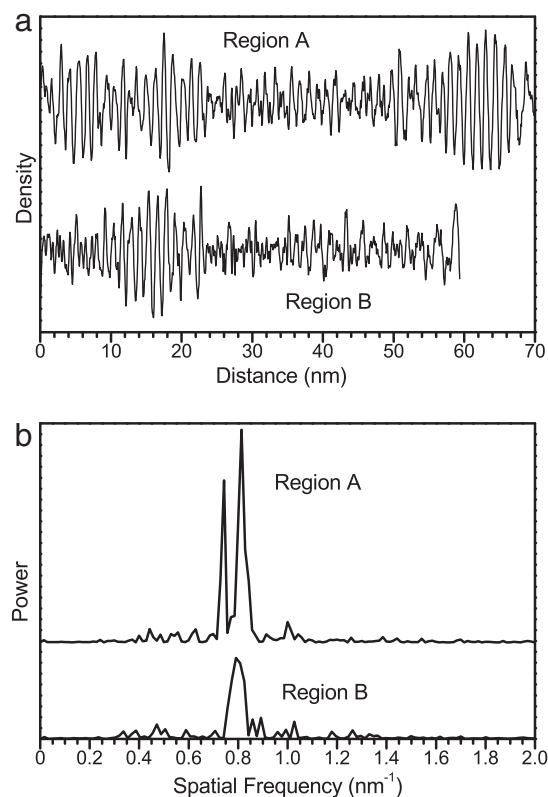

Fig. 7. a) Density profiles of regions A and B in Fig. 6. Distances are measured from left edge of rectangles in Fig. 6. b) Power spectrum of density profiles plotted in panel a.

space peptides limited the extent of contraction. The region B power spectrum exhibited several peaks, all broader and lower in magnitude than the region A peaks. The highest magnitude peaks in the B power spectrum were at 0.560 nm^{-1} (d_{001}-value = 1.79 nm); 0.756 nm^{-1} (d_{001}-value = 1.32 nm); and 0.812 nm^{-1} (d_{001}-value = 1.23 nm). The power spectrum analysis is consistent with the branching and discontinuities observed in the micrographs and plot profiles; region A exhibited more coherent domains with greater uniformity in band spacing; while region B had much less spatial uniformity with smaller coherent domain size. As both A and B regions were part of the same Mt_{TP-10} tactoid, the observed variation in basal spacing and domain size indicated that intercalation can induce greater disorder in the tactoids as well as expansion of the interlayer space. The incidences of peak variability observed in the Fourier spectra from parts of the same tactoid indicated that intercalation is non-uniform. This may have been due to different combinations of peptides being sorbed into separate regions of the aggregate.

At lower tryptone concentration ($Mt_{TP-0.5}$; 0.5 mg/ml solution), quasi-parallel bands were also evident (Fig. 6a). Layers in the central region were sub-parallel and exhibited less contrast which may have represented a more face-on view. Density profiles generated from the regions labeled A and B are plotted in Fig. 7a, with corresponding power spectra shown in Fig. 7b. In the profiles, bands with high contrast between the T–O–T sheets and interlayer space were clustered and extended for approximately 10 layers. This is in contrast to the density profile of the sample intercalated at higher tryptone concentration (Fig. 5a) in which the high contrast density extended over most of the tactoid. The power spectrum from region A exhibited two distinct

peaks. The higher magnitude peak at 0.814 nm^{-1} (d_{001}-value = 1.23 nm) and another peak at 0.743 nm^{-1} (d_{001}-value = 1.35 nm) reflected a variation in interlayer spacing across the tactoid. The larger d_{001} spacing corresponded to the regions nearer to the edges of the particle. The power spectrum of region B, exhibited a broad peak centered at 0.791 nm^{-1} (d_{001}-value = 1.26 nm). Although some domains in the sample exhibited d_{001}-value comparable to the samples intercalated at higher tryptone concentration (Fig. 5b), on average, the d_{001} spacing was smaller in this sample — consistent with XRD results.

A HRTEM micrograph of two, possibly three, tactoids of intercalated $Mt_{TP-0.5}$ in a face-to-face attachment is shown in Fig. 8a. The tactoids underwent intercalation-induced exfoliation in the upper region of the micrograph. The alternating T–O–T sheets and interlayer space bands in inset B (enlarged in Fig. 8b) were organized in a highly parallel orientation with high contrast and a d_{001} spacing of 1.37 nm, exemplifying a coherent crystallite domain extending for 10–15 pairs. Lens-like structures caused by variations in the amount and composition of intercalated peptides were especially visible in inset C (enlarged in Fig. 8c) with branching and pinching. Lateral discontinuities in the layers are indicated by arrows in Fig. 8c. Although HRTEM micrographs show clear evidence of local effects of intercalation in the $Mt_{TP-0.5}$ samples, XRD data indicated that on average the structure of the $Mt_{TP-0.5}$ was the same as non-intercalated Mt.

For comparison, a HRTEM micrograph of a Mt tactoid control in an edge-on orientation is shown in Fig. 9. The d_{001}-value was 1.18 nm, consistent with the d_{001}-value of dehydrated Mt supporting the assumption that plastic resin fixing for TEM dehydrates Mt.
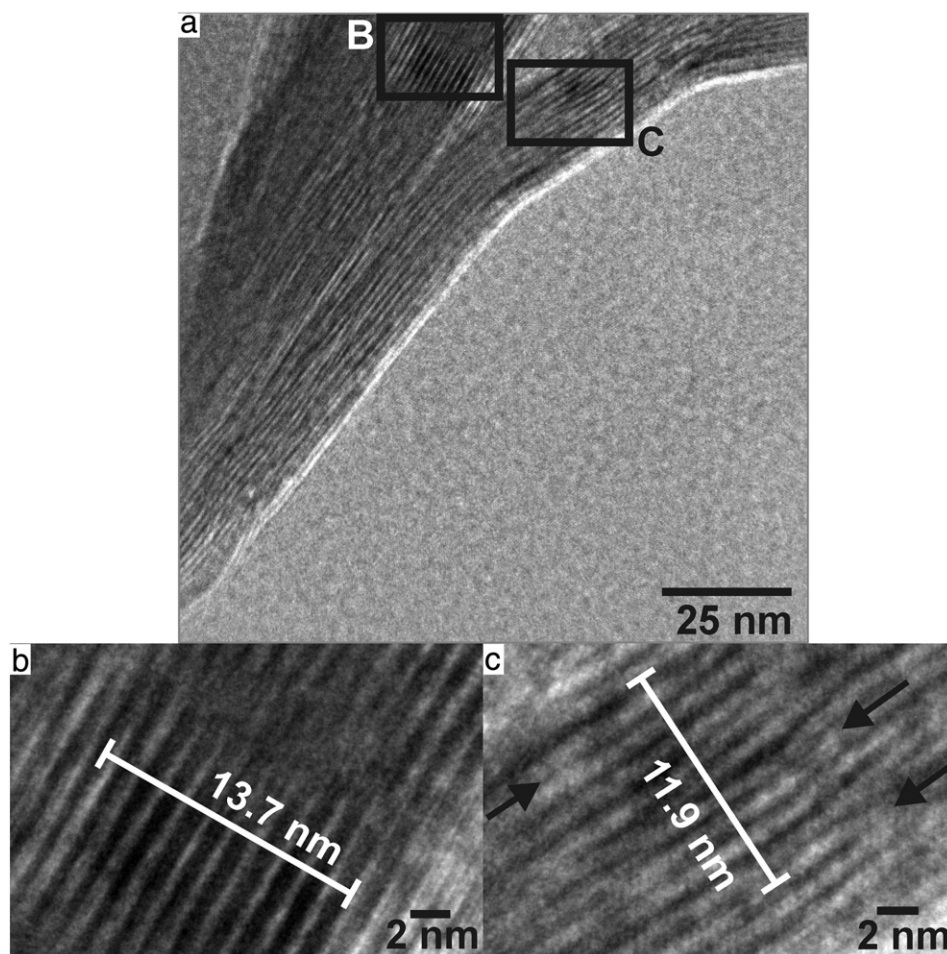
Fig. 8. a) HRTEM of Mt-tryptone aggregate showing curling of the platelets. b, c) Enlarged view of regions in panel a indicated by rectangles labeled B and C, respectively. Lines extend across 10 platelets.
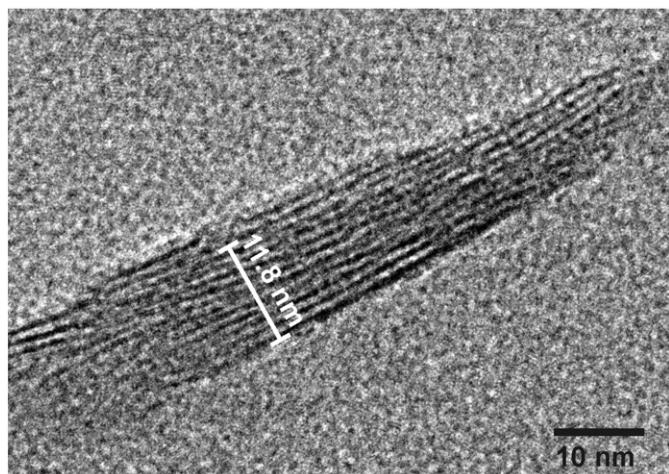
Fig. 9. TEM of Mt without tryptone; d_{001} spacing is 1.18 nm. Line extends across 10 platelets.

3.5. Thermogravimetric analysis

Thermogravimetric and derivative thermogravimetric curves for Mt, Mt_{TP-10} and Mt_{TP-5} are plotted in Fig. 10a and b, respectively. The Mt control exhibited a total mass loss of 14% between 50 °C and 800 °C. Between 50 °C and 200 °C, the mass loss was 8%, corresponding to the loss of most of the surface and interlayer space water. This was followed by a slow 3% mass loss between 200 °C and 550 °C, likely due to dehydration of residual interlayer space water that may have been more tightly bound due to cation bridging. At temperatures above 550 °C, the Mt exhibited a 3% mass loss due to dehydroxylation.
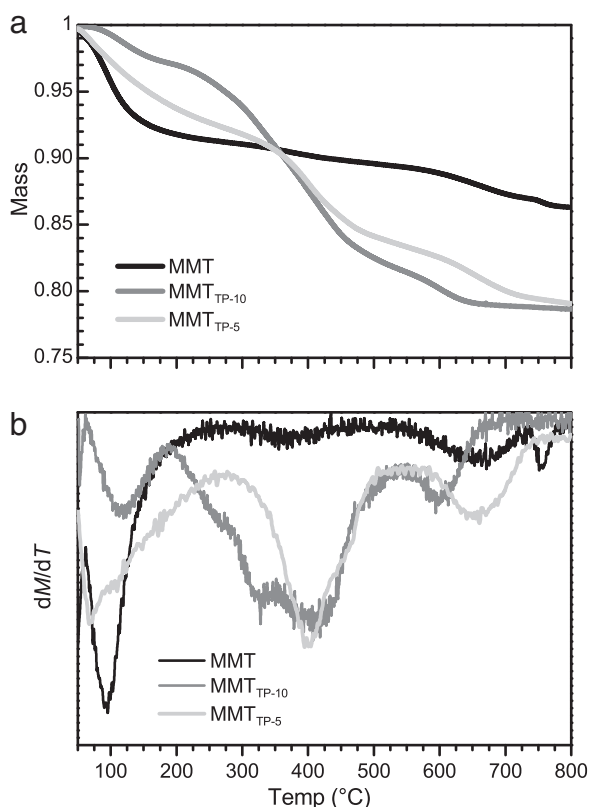
Mt_{TP-10} and Mt_{TP-5} exhibited mass losses between 50 °C and 800 °C of 21.4% and 21.0%, respectively. The consistent mass loss concurs with the UV absorption results that both samples absorbed near equal amounts of tryptone. At lower temperatures, the Mt_{TP-10} experienced a surface water loss of 3% while Mt_{TP-5} did not demonstrate water losses distinguishable from peptide losses. The difference in mass loss between Mt_{TP-5} and Mt_{TP-10} at low temperature was likely due to the effect of ambient humidity on surface water. In these particular samples, the Mt_{TP-5} was more dehydrated at the start of the experiment than the Mt_{TP-10} sample. Due to the variation in amino acid composition and length of peptides, volatilization occurred over a range of temperatures with higher temperatures corresponding to more complex species. At intermediate temperatures (200 °C to 350 °C), the sharper drop in mass in Mt_{TP-5} indicates that a larger fraction of the peptides were surface adsorbed compared to Mt_{TP-10}. The Mt_{TP-10} experienced greater mass loss at higher temperature, indicating that the peptides were more strongly absorbed into the interlayer space.

While an increase in intercalation with tryptone concentration was expected, it was unexpected that the total OM sorbed at both medium (Mt_{TP-5}) and high concentrations (Mt_{TP-10}) was nearly equal. This indicated that the nature of the adsorption is concentration dependent. In Mt_{TP}, surface adsorption was dominant at lower concentrations, followed by absorption into the interlayer space at higher concentration once a layer of OM had been established. This behavior evokes the "onion-layer" model of Sollins et al. (2006), in which mineral surfaces primed with OM promote further adsorption onto unconditioned surfaces. While clay minerals are known to protect OM from microbial degradation to some extent, these results indicate that at a critical peptide concentration, intercalation will supersede surface adsorption resulting in a more stable attachment.

4. Conclusions

The intercalation of small peptides into Mt results in an increase in the d_{001}-value accompanied by exfoliation, edge curling, and poorer crystallinity. XRD results (increased d-spacing with increased peptide concentration) combined with the UV and TGA results (similar relative amount of peptides sorbed by the clay at the 5 mg/ml and 10 mg/ml peptide concentrations) indicate that more peptides are intercalated at the higher concentration. XRD reveals that, on average, significant structural changes occur in the smectite as a result of intercalation. However, high resolution microscopy reveals that intercalation is spatially random, forming multiple crystallite domains with different d_{001} values which are detectable by Fourier analysis of spatial frequencies in the micrographs. The degree to which peptides are adsorbed onto the surface or incorporated into the interlayer space is directly related to the concentration of peptides in solution; while not detectable by XRD at low peptide concentrations, exfoliation and curled edges are observable under HRTEM. At higher concentrations, intercalation is significant, with peptides expanding the basal spacing of the clays and remaining stable at higher temperatures than surface adsorbed peptides. Both surface and intercalated peptides are thermally stable at temperatures above 200 °C, with some intercalated peptides resisting thermal breakdown to temperatures as high as 500 °C. Local variations in interlayer space thickness may depend on the properties of peptides such as molecular mass, charge, or hydrophobicity. TGA and UV absorption results suggest that the OM component derived from peptides in smectites may consist of up to 16% of the total mass. These results indicate that relative peptide concentration dictates whether adsorption to clays will occur predominantly on the surface or on both the surface and in the interlayer space. It can therefore be concluded that at higher peptide concentrations, surface-adsorption mediates interlayer adsorption, leading to increased thermal stability.

Fig. 10. a) TGA of Mt showing fractional mass loss and b) derivative of mass loss.

Acknowledgments

References

Arfaioli, P., Pantani, O.L., Bosetto, M., Ristori, G.G., 1999. Influence of clay minerals and exchangeable cations on the formation of humic-like substances (melanoidins) from D-glucose and L-tyrosine. Clay Miner. 34, 487–497.

Benetoli, L., de Souza, C., da Silva, K., de Souza, I., de Santana, H., Paesano, A., da Costa, A., Zaia, C., Zaia, D., 2007. Amino acid interaction with and adsorption on clays: FT-IR and Mössbauer spectroscopy and X-ray diffractometry investigations. Orig. Life Evol. Biosph. 37, 479–493.

Benincasa, E., Brigatti, M.F., Lugli, C., Medici, L., Poppi, L., 2000. Interaction between glycine and Na-, Ca- and Cu-rich smectites. Clay Miner. 35, 635–641.

Bergaya, F., Lagaly, G., 2013. Handbook of clay science. In: Faïza, B., Gerhard, L. (Eds.), Developments in Clay Science, 2nd ed. Elsevier, p. 813.

Bouchoucha, M., Jaber, M., Onfroy, T., Lambert, J.-F., Xue, B., 2011. Glutamic acid adsorption and transformations on silica. J. Phys. Chem. C 115, 21813–21825.

Bujdák, J., Le Son, H., Rode, B.M., 1996. Montmorillonite catalyzed peptide bond formation: the effect of exchangeable cations. J. Inorg. Biochem. 63, 119–124.

Carneiro, C.E., Berndt, G., de Souza Junior, I.G., de Souza, C.M., Paesano Jr., A., da Costa, A.C., di Mauro, E., de Santana, H., Zaia, C.T., Zaia, D.A., 2011a. Adsorption of adenine, cytosine, thymine, and uracil on sulfide-modified montmorillonite: FT-IR, Mossbauer and EPR spectroscopy and X-ray diffractometry studies. Orig. Life Evol. Biosph. 41, 453–468.

Carneiro, C.E., de Santana, H., Casado, C., Coronas, J., Zaia, D.A., 2011b. Adsorption of amino acids (ALA, CYS, HIS, MET) on zeolites: Fourier transform infrared and Raman spectroscopy investigations. Astrobiology 11, 409–418.

Effenberger, F., Schweizer, M., Mohamed, W.S., 2009. Synthesis and characterization of some polyacrylate/montmorillonite nanocomposites by in situ emulsion polymerization using redox initiation system. J. Appl. Polym. Sci. 112, 1572–1578.

Eusterhues, K., Rumpel, C., Kleber, M., Kögel-Knabner, I., 2003. Stabilisation of soil organic matter by interactions with minerals as revealed by mineral dissolution and oxidative degradation. Org. Geochem. 34, 1591–1600.

Fraser, D.G., Fitz, D., Jakschitz, T., Rode, B.M., 2011. Selective adsorption and chiral amplification of amino acids in vermiculite clay—implications for the origin of biochirality. Phys. Chem. Chem. Phys. 13, 831–838.

Georgelin, T., Jaber, M., Bazzi, H., Lambert, J.-F., 2013. Formation of activated biomolecules by condensation on mineral surfaces — a comparison of peptide bond formation and phosphate condensation. Orig. Life Evol. Biosph. 43, 429–443.

Greenland, D.J., Laby, R.H., Quirk, J.P., 1965a. Adsorption of amino-acids and peptides by montmorillonite and illite. Part 1.—Cation exchange and proton transfer. Trans. Faraday Soc. 61, 2013–2023.

Greenland, D.J., Laby, R.H., Quirk, J.P., 1965b. Adsorption of amino-acids and peptides by montmorillonite and illite. Part 2.—Physical adsorption. Trans. Faraday Soc. 61, 2024–2035.

Harter, R.D., Stotzky, G., 1971. Formation of clay–protein complexes. Soil Sci. Soc. Am. J. 35, 383–389.

Hedges, J.I., Hare, P.E., 1987. Amino acid adsorption by clay minerals in distilled water. Geochim. Cosmochim. Acta 51, 255–259.

Jaber, M., Georgelin, T., Bazzi, H., Costa-Torro, F., Lambert, J.-F., Bolbach, G., Clodic, G., 2014. Selectivities in adsorption and peptidic condensation in the (arginine and glutamic acid)/montmorillonite clay system. J. Phys. Chem. C 118, 25447–25455.

Jaisi, D.P., Eberl, D.D., Dong, H., Kim, J., 2011. The formation of illite from nontronite by mesophilic and thermophilic bacterial reaction. Clays Clay Miner. 59, 21–33.

Jonas, E.C., Oliver, R.M., 1967. Size and shape of montmorillonite crystallites. Clays Clay Miner. 15, 27–33.

Kalra, S., Pant, C.K., Pathak, H.D., Mehata, M.S., 2003. Studies on the adsorption of peptides of glycine/alanine on montmorillonite clay with or without co-ordinated divalent cations. Colloids Surf. A 212, 43–50.

Keller, W.D., Reynolds, R.C., Inoue, A., 1986. Morphology of clay minerals in the smectite-to-illite conversion series by scanning electron microscopy. Clays Clay Miner. 34, 187–197.

Kim, J., Dong, H., Seabaugh, J., Newell, S.W., Eberl, D.D., 2004. Role of microbes in the smectite-to-illite reaction. Science 303, 830–832.

Kleber, M., Mikutta, R., Torn, M.S., Jahn, R., 2005. Poorly crystalline mineral phases protect organic matter in acid subsoil horizons. Eur. J. Soil Sci. 56, 717–725.

Kleber, M., Sollins, P., Sutton, R., 2007. A conceptual model of organo-mineral interactions in soils: self-assembly of organic molecular fragments into zonal structures on mineral surfaces. Biogeochemistry 85, 9–24.

Kollár, T., Pálinkó, I., Kónya, Z., Kiricsi, I., 2003. Intercalating amino acid guests into montmorillonite host. J. Mol. Struct. 651–653, 335–340.

Lagaly, G., 2006. Colloid clay science. In: Bergaya, F., Theng, B.K.G., Lagaly, G. (Eds.), Handbook of Clay Science. Elsevier, pp. 141–246.

Laird, D.A., Martens, D.A., Kingery, W.L., 2001. Nature of clay–humic complexes in an agricultural soil. Soil Sci. Soc. Am. J. 65, 1413–1418.

Lambert, J.F., 2008. Adsorption and polymerization of amino acids on mineral surfaces: a review. Orig. Life Evol. Biosph. 38, 211–242.

Lee, S.Y., Kim, S.J., 2002a. Expansion characteristics of organoclay as a precursor to nano-composites. Colloids Surf. A Physicochem. Eng. Asp. 211, 19–26.

Lee, S.Y., Kim, S.J., 2002b. Transmission electron microscopy of hexadecyltrimethyl-ammonium-exchanged smectite. Clay Miner. 37, 465–471.

Leser, V., Drobne, D., Pipan, Z., Milani, M., Tatti, F., 2009. Comparison of different preparation methods of biological samples for FIB milling and SEM investigation. J. Microsc. 233, 309–319.

Mayer, L.M., 1994. Relationships between mineral surfaces and organic carbon concentrations in soils and sediments. Chem. Geol. 114, 347–363.

Moore, D., Reynolds Jr., R.C., 1997. X-ray Diffraction and the Identification and Analysis of Clay Minerals. 2nd ed. Oxford University Press, New York.

Naidja, A., Huang, P.M., 1994. Aspartic acid interaction with Ca-montmorillonite: adsorption, desorption and thermal stability. Appl. Clay Sci. 9, 265–281.

Olafsson, P., Bryan, A., 1970. Evaluation of thermal decomposition temperatures of amino acids by differential enthalpic analysis. Microchim. Acta 58, 871–878.

Parbhakar, A., Cuadros, J., Sephton, M.A., Dubbin, W., Coles, B.J., Weiss, D., 2007. Adsorption of L-lysine on montmorillonite. Colloids Surf. A 307, 142–149.

Rillig, M.C., Caldwell, B.A., Wösten, H.B., Sollins, P., 2007. Role of proteins in soil carbon and nitrogen storage: controls on persistence. Biogeochemistry 85, 25–44.

Senwo, Z.N., Tabatabai, M.A., 1998. Amino acid composition of soil organic matter. Biol. Fertil. Soils 26, 235–242.

Sheng, G., Johnston, C.T., Teppen, B.J., Boyd, S.A., 2001. Potential contributions of smectite clays and organic matter to pesticide retention in soils. J. Agric. Food Chem. 49, 2899–2907.

Sollins, P., Homann, P., Caldwell, B.A., 1996. Stabilization and destabilization of soil organic matter: mechanisms and controls. Geoderma 74, 65–105.

Sollins, P., Swanston, C., Kleber, M., Filley, T., Kramer, M., Crow, S., Caldwell, B.A., Lajtha, K., Bowden, R., 2006. Organic C and N stabilization in a forest soil: evidence from sequential density fractionation. Soil Biol. Biochem. 38, 3313–3324.

Sterte, J., Shabtai, J., 1987. Cross-linked smectites. V. Synthesis and properties of hydroxy-silicoaluminum montmorillonites and fluorhectorites. Clays Clay Miner. 35, 429–439.

Stoscheck, C.M., 1990. Quantitation of protein. In: Murray, P.D. (Ed.), Methods in Enzymology. Academic Press, pp. 50–68.

Theng, B.K.G., 1982. Clay polymer interactions: summary and perspectives. Clays Clay Miner. 30, 1–10.

Theng, B.K.G., 2012. Formation and Properties of Clay–Polymer Complexes. 2nd ed. Elsevier Science, Amsterdam.

Xi, Y., Ding, Z., He, H., Frost, R.L., 2004. Structure of organoclays—an X-ray diffraction and thermogravimetric analysis study. J. Colloid Interface Sci. 277, 116–120.

Xu, M., 2003. Light extinction and absorption by arbitrarily oriented finite circular cylinders by use of geometrical path statistics of rays. Appl. Opt. 42, 6710–6723.

Xu, M., Katz, A., 2008. Statistical interpretation of light anomalous diffraction by small particles and its applications in bio-agent detection and monitoring. In: Kokhanovsky, A.A. (Ed.), Light Scattering Reviews. 3. Springer, Chichester, UK, pp. 27–67.

Xu, M., Lax, M., Alfano, R.R., 2003. Anomalous diffraction of light with geometrical path statistics of rays and a Gaussian ray approximation. Opt. Lett. 28, 179–181.

Yu, W.H., Li, N., Tong, D.S., Zhou, C.H., Lin, C.X., Xu, C.Y., 2013. Adsorption of proteins and nucleic acids on clay minerals and their interactions: a review. Appl. Clay Sci. 80–81, 443–452.

Zhang, G., Dong, H., Kim, J., Eberl, D.D., 2007a. Microbial reduction of structural Fe^{3+} in nontronite by a thermophilic bacterium and its role in promoting the smectite to illite reaction. Am. Mineral. 92, 1411–1419.

Zhang, G., Kim, J., Dong, H., Sommer, A.J., 2007b. Microbial effects in promoting the smectite to illite reaction: role of organic matter intercalated in the interlayer. Am. Mineral. 92, 1401–1410.